



### 3-Dimensional analysis of fatigue crack fields and crack growth by in situ synchrotron X-ray tomography

A. Koko<sup>a</sup>, S. Singh<sup>a</sup>, S. Barhli<sup>a</sup>, T. Connolley<sup>b</sup>, N.T. Vo<sup>b</sup>, T. Wigger<sup>c</sup>, D. Liu<sup>d</sup>, Y. Fu<sup>a</sup>, J. Réthoré<sup>e</sup>, J. Lechambre<sup>e</sup>, J.-Y. Buffiere<sup>e</sup>, T.J. Marrow<sup>a,\*</sup>

<sup>a</sup> University of Oxford, Department of Materials, Parks Rd, Oxford, UK

<sup>b</sup> Diamond Light Source, Harwell Science and Innovation Campus, Fermi Ave, Didcot OX11 0DE, UK

<sup>c</sup> University College London, Department of Mechanical Engineering, Torrington Place, London WC1E 7JE, UK

<sup>d</sup> University of Bristol, Department of Physics, Tyndall Avenue, Bristol BS8 1TL, UK

<sup>e</sup> INSA Lyon, Avenue Jean Capelle 69621 Villeurbanne, France

#### ARTICLE INFO

##### Keywords:

Cast iron  
Crack closure  
Crack growth rate  
Elliptical cracks  
Stress intensity factors

#### ABSTRACT

The propagation rate of a fatigue crack in a nodular cast iron, loaded in cyclic tension, has been studied in situ by X-ray computed tomography and digital volume correlation. The semi-elliptical crack initiated from an asymmetric corner notch and evolved to a semi-circular shape, initially with a higher growth rate towards one edge of the notch before the propagation rate along the crack front became essentially independent of position. The phase congruency of the displacement field was used to measure the crack shape. The three-dimensional stress intensity factors were calculated via a linear elastic finite element model that used the displacement fields around the crack front as the boundary conditions. Closure of the crack tip region was observed. The cyclic change in the local mode I opening of the crack tip determined the local fatigue crack propagation rate along the crack front.

#### 1. Introduction

Crack propagation by metal fatigue occurs as a direct consequence of the cyclic strains at the crack tip. The basic mechanism has been known and understood for decades, yet problems remain in the accurate prediction of fatigue crack growth rates in engineering components despite the existence of quite sophisticated models. Lack of confidence in the general application of these models leads to over-conservatism in structural integrity assessments, with a significant economic cost, particularly in the aviation and nuclear energy sectors.

It is possible to accurately define in engineering designs (and to control in experiments) the loading applied to a cracked component and to measure precisely the average crack propagation rate of the crack front; however, the behaviour of cracks is very sensitive to the load history. Fatigue models [1] have therefore become quite complex in the attempt to describe the effects of strain gradients, residual stress, overloads, spectrum loading, and so on, which all arise in real engineering applications. Whilst these models can be applied with some success in engineering design, there are problems of transferability between materials and material conditions. This increases the costs of introducing

new materials and manufacturing processes to fatigue critical components, and to stress states and histories that have not been, or cannot be, examined empirically by experiment.

A significant factor in this problem is that the cyclic strains at the crack tip, which result from the applied loads and cause crack propagation [2], are dependent on the local elastic and plastic deformation field around the crack tip [3]. The properties of the crack tip plastic zone depend on its strain history and the strain state that it experiences, so a complex coupling exists between the applied boundary conditions and the local deformations that cause crack growth [4]: the plastic zone has further effects such as the development of compressive closure stresses behind the crack tip [5]. Environmental factors, which depend critically on crack tip deformation, are also highly complex to address [6].

A substantial barrier to the validation of models for fatigue, and also fracture, is the difficulty of accurately measuring both the local deformation conditions and the crack's response. Until recently, their simultaneous measurement has only been possible at the surface by imaging (i.e. digital image correlation) [7–11] or scattering [12,13], although internal measurements of the crack's elastic strain field have been obtained by diffraction in transmission [14–16]. Attenuation

\* Corresponding author.

E-mail address: [james.marrow@materials.ox.ac.uk](mailto:james.marrow@materials.ox.ac.uk) (T.J. Marrow).

<https://doi.org/10.1016/j.ijfatigue.2023.107541>

Received 28 October 2022; Received in revised form 19 January 2023; Accepted 23 January 2023

Available online 28 January 2023

0142-1123/© 2023 The Authors. Published by Elsevier Ltd. This is an open access article under the CC BY license (<http://creativecommons.org/licenses/by/4.0/>).

contrast from features in the microstructure can allow the use of digital volume correlation (DVC) to map the relative changes in the displacement field between tomographic datasets. This makes it possible to measure directly the three-dimensional (3D) displacements of the material surrounding the crack, the total strains around the crack tip, and also the resulting crack opening profile up to the crack tip (e.g. [17–19]). One critical experiment [20] studied the propagation of a short fatigue crack in a match-stick sample ( $1.6 \text{ mm} \times 1.6 \text{ mm}$ ) of nodular cast iron by high resolution synchrotron X-ray computed tomography (XCT). This was the first time values of the stress intensity factor range were extracted from experimentally measured displacements along the front of a fatigue crack *within* an optically opaque material. A subsequent study [21] determined the evolution of the local stress intensity factors in a short semi-elliptical crack propagating in a match-stick sample of similar material, by fitting the measured displacements to the Williams solution for elastic deformation [22] with an iterative method applied to determine the effective crack tip position.

An analysis has been developed [23–26], which uses a finite element method that is less sensitive to the determination of the crack tip position [27,28]. This also enables the treatment of non-linear material properties [29] and mixed-mode loading [9]. Initially applied to two-dimensional (2D) studies [30,31], it has been extended to 3D observations of deformation and damage that can be obtained by in situ high-resolution XCT. Using information of the displacement field, and without requiring knowledge of the applied loads or crack geometry, a finite element simulation can be used to calculate the elastic strain energy release rate (J-integral) via the virtual crack extension/domain integral [32]. Under small-scale yielding conditions (i.e., linear elasticity), the local mode I, II and III stress intensity factors acting on the crack tip can then be obtained [33,34] by using the interaction integral [35] that is natively implemented in finite element solvers such as Abaqus/Standard.

The objective of this study was to measure the cyclic displacement field acting on a propagating three-dimensional crack of complex shape and to parameterise this deformation by a local stress intensity factor range that could be related to the crack's response (i.e., the local crack growth rate). The measurements were achieved using high-energy, limited-angle, synchrotron XCT to observe a mm-sized semi-elliptical fatigue crack propagating from the corner of a large square-section specimen ( $\sim 5 \text{ mm}$ ) of nodular cast iron, loaded in cyclic tension. The microstructure's graphite nodules allowed high-resolution digital volume correlation of the tomographs, recorded in situ, to measure the relative displacements. The 3D displacements were also used to determine the crack shape, via the phase congruency of the displacement field, and to calculate the variation of the local stress intensity factor

range acting on the crack tip with load and number of cycles.

## 2. Materials and experimental method

The material was a custom-made nodular graphite cast iron, previously studied using high resolution X-ray tomography [21,36,37]; a similar material was also used in an earlier tomography study of fatigue initiation [38]. The billet used to create the specimen contained 3.4 wt% carbon and was ferritised at  $880^\circ\text{C}$  then air quenched. This material is particularly suitable for DVC analysis as it contains 14 vol% of graphite nodules of an average diameter of  $45 \mu\text{m}$  that give strong X-ray attenuation contrast. The specimen preparation was in two steps; first, the cylindrical shape was cut using conventional machining, then an electro-discharge machining (EDM) tool was used to cut the central gauge section and the notch, using a round wire that gave a notch tip diameter close to  $300 \mu\text{m}$  (Fig. 1a). The notch was cut at one corner of the square section gauge length, perpendicular to the specimen axis, with the notch tip at an angle of  $35^\circ$  to one surface. This gave surface lengths of 1.25 mm and 0.88 mm on the adjacent surfaces. The purpose was to develop non-uniform loading along the notch tip that would affect the initial propagation of the crack.

The in situ fatigue study was performed on the I12 Joint Engineering, Environmental and Processing (JEEP) beamline at the UK Diamond Light Source synchrotron [39]. The specimen was fatigue loaded using a 100 kN Instron uniaxial servo-hydraulic mechanical test rig at a cyclic frequency of 15 Hz and the ratio of maximum to minimum load (R-ratio) of 0.1. A razor blade was run across the notch tip before loading. Pre-tests were done to establish suitable loading conditions to initiate and propagate a fatigue crack from the notch (Fig. 1b). At intervals, the cycling was suspended, and the specimen was observed by tomography.

A monochromatic beam of energy 80 keV was used, and radiographs were recorded using the PCO.4000 CCD camera ( $2560 \times 2160$  pixels, 16-bit depth), with module 3 optics selected to image an area of  $8.3 \times 7.0 \text{ mm}$  (i.e.  $3.24 \mu\text{m}$  per pixel). The time per tomograph was 10 min, with an exposure time per radiograph of 0.2 s, recording 3000 radiographs over an angular range from  $-80.4^\circ$  to  $+62^\circ$ . This was necessary due to the blocking of X-ray transmission by the vertical load columns of the Instron. The reconstruction of the tomographs used the I12 beamline software, which implemented back-filtered projection with Fourier-wavelet ring artefact removal. No special adjustments were made for the limited angle of data collection.

In Stage I of the experiment, the initiation and propagation of the crack from the notch was studied with tomographs recorded at intervals from 50,000 to 290,000 cycles at the maximum load ( $P_{\max}$  4.5 kN) and minimum load ( $P_{\min}$  0.45 kN). After 290,000 cycles, the opening and

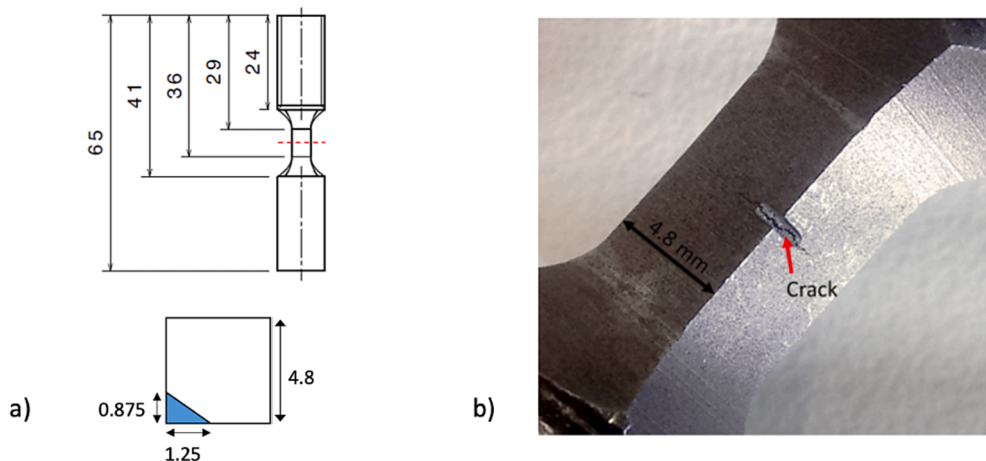


**Fig. 1.** Fatigue specimen: a) dimensions and square cross-section (4.8 mm) with asymmetric corner notch (0.3 mm width); b) optical image of the notch and a fully developed crack from a pre-test that was performed to establish the experimental conditions for the in situ experiment.

closing behaviour of the developed crack was studied by a series of tomographs recorded in steps over a single cycle with increasing load from 0.45 to 4.5 kN, then with decreasing load.

In Stage II and Stage III of the experiment, the potential effect of crack closure was studied by reducing the cyclic range to verify crack arrest, and then increasing the cyclic range to reinitiate crack growth. As in Stage I, tomographs were obtained at both minimum ( $P_{min}$ ) and maximum ( $P_{max}$ ) loads. In Stage II, with the load range reduced by 40% (i.e. 0.3 kN to 3 kN), scans were obtained at intervals up to a total of 500,000 cycles. Then, in Stage III, at an increased load range (0.35 kN to 3.5 kN), tomography scans were obtained at intervals up to 625,000 cycles in total. The total number of fatigue cycles was counted from the start of the experiment at the beginning of Stage I.

DVC analysis of the tomographs was performed using the LaVision DaVis StrainMaster 8.2 software on a dedicated workstation (Intel Xeon E5-2699 v3, 2x 18 cores @ 2.3 GHz, 512 Gb RAM). The reference was always the tomograph recorded at the minimum load at the same number of fatigue cycles. The analysis used the direct correlation mode with iterative reduction of the subset size from  $96 \times 96 \times 96$  voxels to smaller subsets with dimensions of 64, 48, and 32 voxels using 75% overlap and 2 passes at each stage. Residual rigid body translation and rotation of the specimen was removed from the displacement field using a method [40] implemented in Matlab, with the final displacements defined relative to an origin at the centre of the notch plane.

### 3. Results

During Stage I ( $P_{min}$  0.45 kN,  $P_{max}$  4.5 kN), cracks were observed to have initiated at the surface of the blunt notch after  $\sim 50,000$  cycles, and these coalesced to form a single crack by  $\sim 100,000$  cycles. Fig. 2a shows an example cross-section at 75,000 cycles, close to and parallel to the notch tip, which reveals a set of coalescing short cracks. Fig. 2b shows a series of sections perpendicular to the notch between 190,000 and 290,000 cycles to illustrate the progressive propagation of the crack, which was parallel to the notch plane. A cross-section of the crack (central and perpendicular to the notch tip) at the end of Stage I

(290,000 cycles) is shown in Fig. 3, where it can be compared with the same section at the beginning (290,000 cycles) and end (500,000 cycles) of Stage II, and then at 550,000 and 600,000 cycles in Stage III. In each case, the crack was imaged at the relevant maximum load. There was no detectable crack growth during Stage II when the load range was reduced ( $P_{min}$  0.3 kN,  $P_{max}$  3.0 kN), but the crack propagated by  $\sim 150 \mu\text{m}$  during Stage III once the load range was increased ( $P_{min}$  0.35 kN,  $P_{max}$  3.5 kN).

Fig. 4 shows an example of the three-dimensional displacement field measured by digital volume correlation at 290,000 cycles (i.e. at the end of Stage I and the beginning of Stage II). The field presents the component of the displacement change ( $\Delta U_z$ ) parallel to the loading axis, between the minimum and maximum loads. The opening displacements are of the order of  $10 \mu\text{m}$  at the notch mouth. The shear displacements ( $\Delta U_x$  and  $\Delta U_y$ ) were negligible in comparison. Measurements of the locus of the crack tip in the notch plane at 290,000 cycles are shown in Fig. 5a. The crack tip position was determined by i) manual identification from image contrast in slices of the XCT image; ii) using a strain threshold of 0.15 (maximum normal 3D strain) measured from the gradient of the displacement field; and iii) phase congruency of the 3D displacement field [24,34]. Both ii) and iii) are sensitive to the opening of the crack. Crack segmentation by visual examination, which in principle has a resolution of a few voxels, was quite difficult and prone to uncertainty due to the low contrast of the crack and the complex microstructure. The strain threshold analysis used the DVC displacement field obtained with the smallest  $32 \times 32 \times 32$  voxel subset analysis, but the choice of strain threshold, which can affect the apparent crack tip position, was subjective. The crack tip defined using the strain threshold tends to over-estimate the crack length at low  $\theta$  and under-estimate at high  $\theta$ , compared with the manual measurements. The phase congruency method [24] is not subjective as it determines the location at which the Fourier components of the displacement field are most in phase. The phase congruency analysis used the DVC displacement field obtained for the  $48 \times 48 \times 48$  subset analysis; the displacement noise at the smaller 32 voxel subset introduced higher uncertainty, whereas larger subsets had a lower spatial resolution. The maximum spatial resolution of the

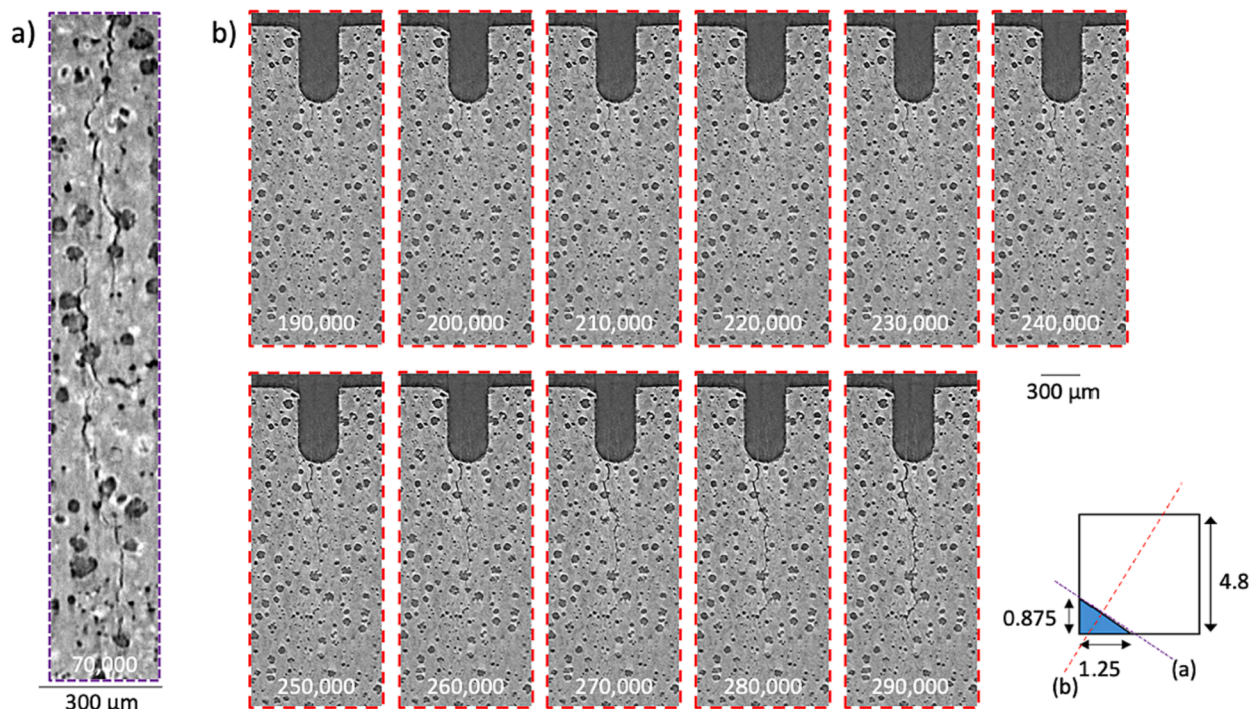
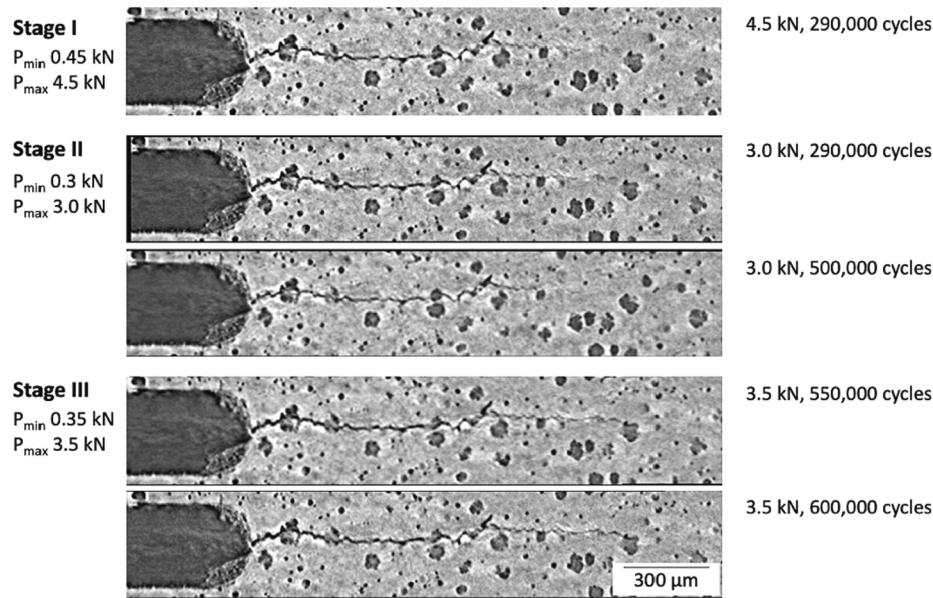
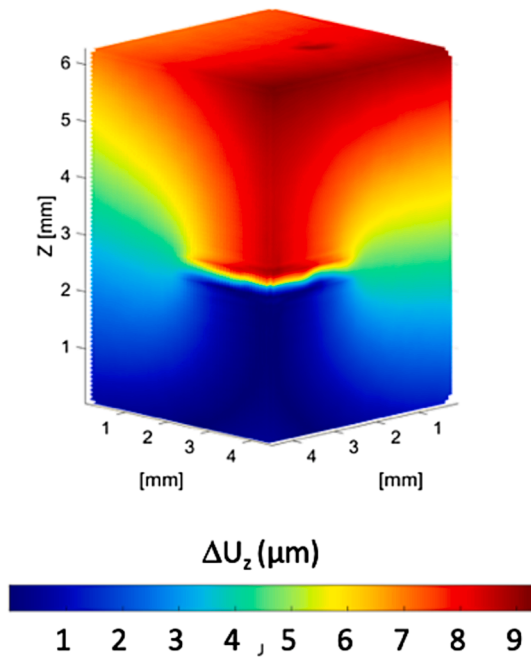


Fig. 2. X-ray tomograph virtual sectioning: a) section parallel to the notch tip at 75,000 cycles; b) series of sections perpendicular to the notch between 190,000 and 290,000 cycles. The traces of the a) and b) sections relative to the notch are indicated.





**Fig. 3.** Tomography virtual section of the crack imaged at maximum load at the end of Stage I (290,000 cycles), at the beginning (290,000 cycles) and end (500,000 cycles) of Stage II, and at 550,000 and 600,000 cycles in Stage III. In each case, the crack is imaged at the maximum load of the respective stage.



**Fig. 4.** The three-dimensional displacement field ( $\Delta U_z$ , parallel to the specimen loading direction) measured by digital volume correlation ( $96 \times 96 \times 96$  subset, 75% overlap) at 290,000 cycles.

phase congruency and strain threshold measurements depends on the separation of the displacement vectors measured by DVC, which were 12 voxel ( $\sim 40 \mu\text{m}$ ) and 8 voxel ( $26 \mu\text{m}$ ), respectively. The phase congruency measurement shows good agreement with the manual measurement from the X-ray tomographs and tends to find a smoother locus of the crack tip.

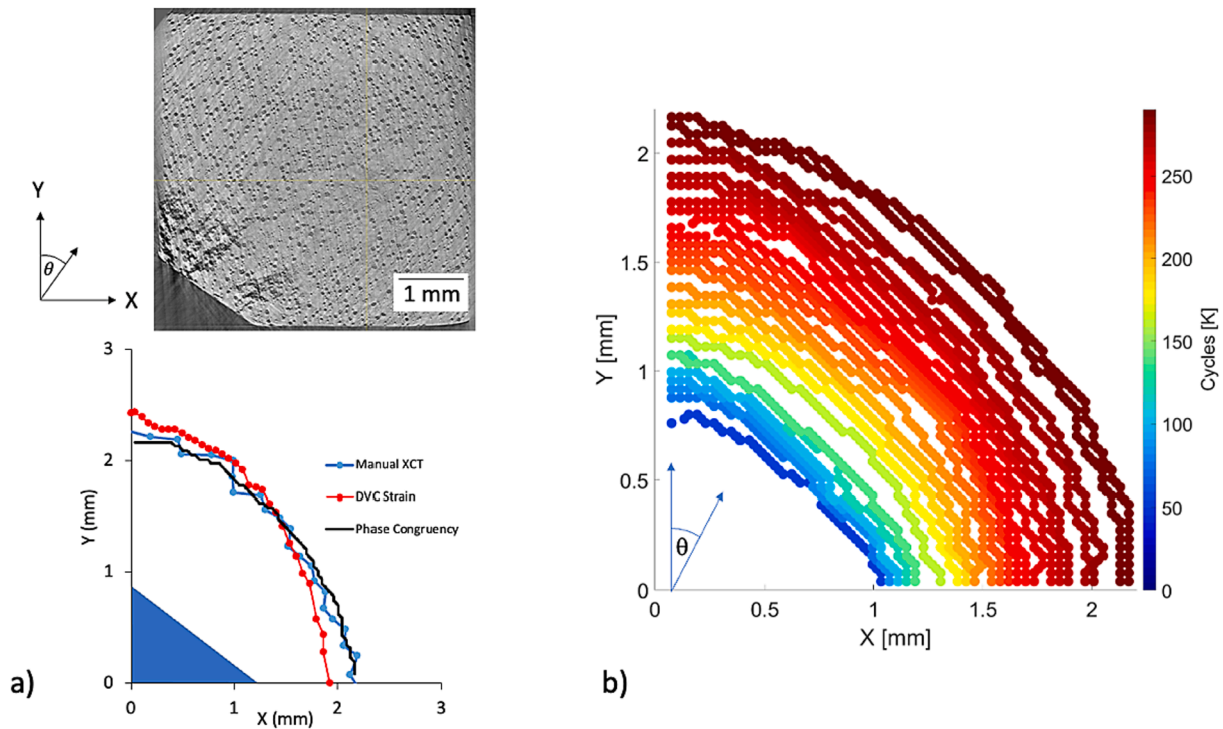
The crack tip positions obtained by phase congruency were used to determine the progressive evolution of the crack (Fig. 5b). The local crack growth rates are shown in Fig. 6 as a function of the angular position,  $\theta$ , around the crack front (defined in Fig. 5). The trace of the crack tip position is projected onto the notch plane, and since cracks were

initiated at different locations around the circumference of the blunt tip (Fig. 2) the crack dimension can appear shorter than the maximum extent of the notch tip at low numbers of cycles. The crack growth rate,  $da/dN$ , was calculated using the local increments between observations of the crack tip position [19]. The average gradient over 3 or more observations was generally used to reduce noise, but as the crack growth rate increased towards the end of Stage I the gradient between successive observations was used. Fig. 6 shows that the crack growth rate increased with the number of cycles and tended to be higher towards lower values of  $\theta$ , particularly in the observations below 200,000 cycles.

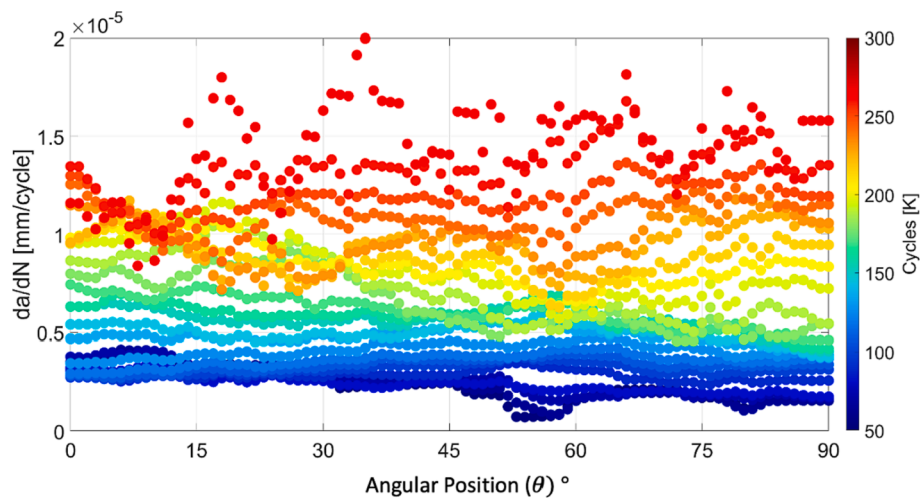
The displacement field change, measured by DVC between the minimum and maximum loads at the same number of cycles, was used to evaluate the local stress intensity factor range at the crack tip. For higher precision of the displacements, the DVC dataset obtained at  $96 \times 96 \times 96$  voxel subset was used as the boundary conditions that were applied to the nodes of a finite element model [33,34] (hexahedral mesh with 8 nodes per element) within Abaqus/Standard. The crack was defined as a planar feature, perpendicular to the specimen axis (i.e. parallel to the notch), with the position of its curved tip identified using the phase congruency analysis. The crack's elastic field was evaluated as the J-integral for a virtual crack extension by considering a set of two-dimensional plane strain sections in radial directions that were defined by their angular position,  $\theta$  (Fig. 5b). The elastic properties assumed in the model were linear and isotropic, with Young Modulus  $E = 158 \text{ GPa}$  and Poisson ratio  $\nu = 0.3$  [41]. Using the domain integral analysis tools in Abaqus/Standard, the equivalent stress intensity factor,  $K_{eqv}$ , was obtained from the J-integral and the mixed mode stress intensity factors ( $K_I$ ,  $K_{II}$  and  $K_{III}$ ) were then extracted using the interaction integral.

Fig. 7b shows an example of the evaluation of the crack tip field for the 2D section at the angular position  $\theta = 45^\circ$  (i.e. the strain energy release rate was calculated at one location along the crack tip for a virtual crack extension in the  $45^\circ$  direction that was approximately orthogonal to the crack front). Convergence was obtained with increasing contour number as the integration domain increased in size. The shear modes ( $K_{II}$  and  $K_{III}$ ) of the stress intensity factor were negligible. The converged value of the change in  $K_I$  relative to the reference tomograph was taken as the local mode I stress intensity factor range ( $\Delta K_I$ ) between the minimum and maximum loads. The variation of  $\Delta K_I$  as a function of propagation direction around the crack tip (i.e. the





**Fig. 5.** Measurements of the locus of the crack tip in the notch plane: a) at 290,000 cycles by manual identification from the XCT image ('Manual XCT'), a DVC strain threshold ('DVC Strain') and phase congruency of the DVC displacement field ('Phase Congruency'); b) progressive evolution with fatigue cycles of the crack, measured by phase congruency from 50,000 to 290,000 cycles in Stage I. The angular position,  $\theta$ , is defined relative to the Y-axis and the specimen corner. The data are colour-coded by the number of fatigue cycles. The example X-Y slice of the XCT data is at the central plane of the notch at maximum load,  $P_{max}$ , at 290,000 cycles.



**Fig. 6.** The crack growth rate during Stage I, orthogonal to the crack front, as a function of the angle  $\theta$  around the crack front (as defined in Fig. 5). The data are colour-coded by the number of fatigue cycles.

angular position,  $\theta$ ) is summarized in Fig. 8 for increasing numbers of cycles. The figure shows that  $\Delta K_I$  tended to increase with increasing numbers of cycles and was higher towards lower values of  $\theta$ . The individual data points are the mean of the values in the converged region (i. e. beyond contour 10 in this case), and the error bars are their standard deviation.

The crack and its local stress intensity factor range were examined in detail using the observations obtained over one individual cycle at 290,000 load cycles. The series of images (Fig. 9a) in which the tomographs of the crack have been sectioned at  $\theta = 45^\circ$  shows that the crack tip is more visible as the load increases, and the visible crack length tends to increase. The open crack tip position, which was identified

using the phase congruency of the displacement field, also moves forwards as the maximum load is approached (Fig. 9b). The mode I stress intensity factor range,  $\Delta K_I$ , was evaluated relative to the minimum load ( $P_{min}$  0.45 kN) as the crack was loaded and then unloaded, with the constant crack tip taken at its furthest position (i.e. identified by phase congruency at the maximum load,  $P_{max}$  4.5 kN). The variation of  $\Delta K_I$  as a function of angular position  $\theta$  with increasing load is presented in Fig. 10a, and the value of  $\Delta K_I$  at  $\theta = 45^\circ$  as a function of applied load is summarised in Fig. 10b as an example. This figure shows  $\Delta K_I$  did not increase significantly until the maximum load exceeded 4 kN, and a similar significant change in  $\Delta K_I$  between 4 and 4.5 kN can be observed along the whole crack front. The values of  $\Delta K_I$  with during unloading

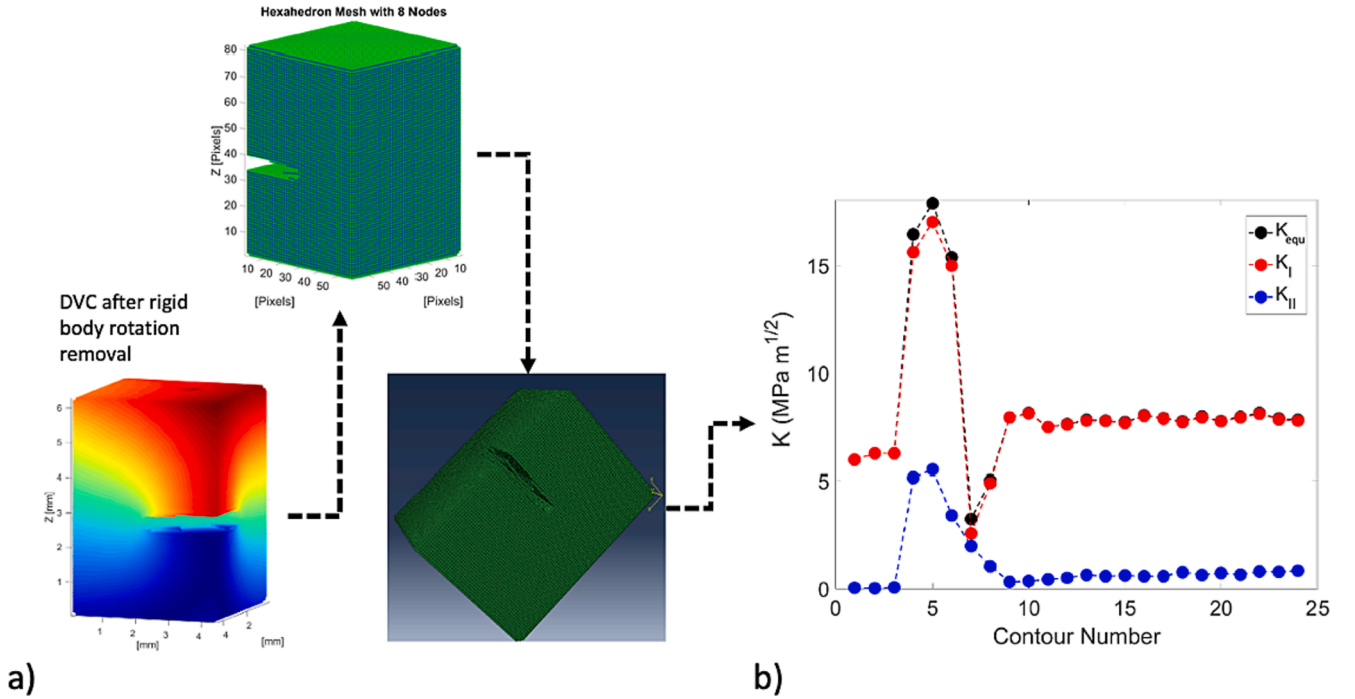


**Fig. 7.** Calculation of local stress intensity factors: a) DVC displacement field applied as boundary conditions in a finite element model (hexahedral mesh with 8 nodes per element); b) example of convergence with increasing integration domain size (contour number) of the equivalent stress intensity factor,  $K_{\text{equ}}$ , separated into mode I and mode II components ( $K_I$  and  $K_{II}$ ) using the interaction integral. The mode III component was negligible.

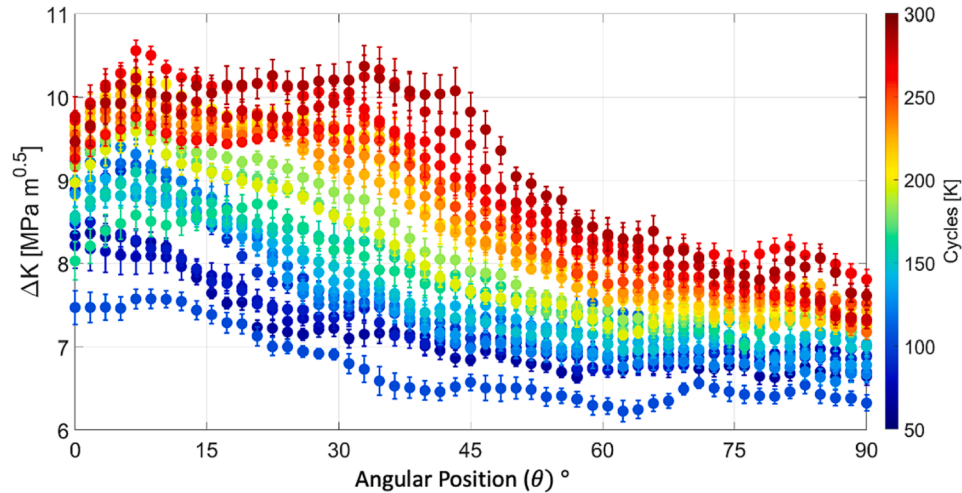


**Fig. 8.** Variation of the mode I stress intensity factor range  $\Delta K_I$  as a function of propagation direction (i.e. the angular position  $\theta$  around the crack front) for increasing numbers of cycles in Stage I. The data are colour-coded by the number of fatigue cycles.

were close to those during loading. At loads below 4 kN, the value of  $\Delta K_I$  did increase to some extent with load, and the effect was smallest at higher angular positions. Sections of the tomograph at  $P_{\text{max}}$  (4.5 kN) at 290,000 cycles (Fig. 10c) close to the surface near  $\theta = 0^\circ$  and  $\theta = 90^\circ$  show the crack was discontinuous (i.e. bridged) in the region close to  $\theta = 90^\circ$ , but no such bridges were observed elsewhere.

The relation between the local crack growth rate and the local  $\Delta K_I$  calculated from the displacement change between the minimum and maximum load during Stage I is shown in Fig. 10, which uses the data from Fig. 6 and Fig. 8. The data points have been colour-coded by their angular position,  $\theta$ , and a simple Paris-Erdogan equation  $\frac{da}{dN} = A(\Delta K_I - \Delta K_{th})^P$  [42] has been fitted to the full dataset. The threshold stress intensity factor range,  $\Delta K_{th}$ , was fixed at  $6.2 \text{ MPa m}^{1/2}$  by inspection, then the other constants were obtained by least squares

optimisation to obtain  $A = 4.4 \pm 0.1 \times 10^{-6} \text{ mm/cycle}$  and the Paris exponent  $P = 0.81 \pm 0.03$ . The confidence of the fit to the data is only moderate, at  $R^2 = 0.50$ , and for an equivalent  $\Delta K_I$  there is a strong tendency at high  $\theta$  for higher growth rates. Noting from Fig. 10b that  $\Delta K_I$  did not increase significantly until the maximum load exceeded 4 kN, the crack growth rate at  $\sim 290,000$  cycles (Fig. 6) is shown in Fig. 11b as a function of the local change in  $K_I$  between 4 and 4.5 kN, using the stress intensity factors calculated along the crack front (Fig. 10a). These data form a cluster with similar values of growth rate and  $\Delta K_I$  without a strong effect of angular position. The growth rates are comparable to those observed at similar stress intensity factors for smaller fatigue cracks in the same material [21].

The stress intensity factor range was also calculated using the standard relations for a corner crack under tensile loading [43,44] that use

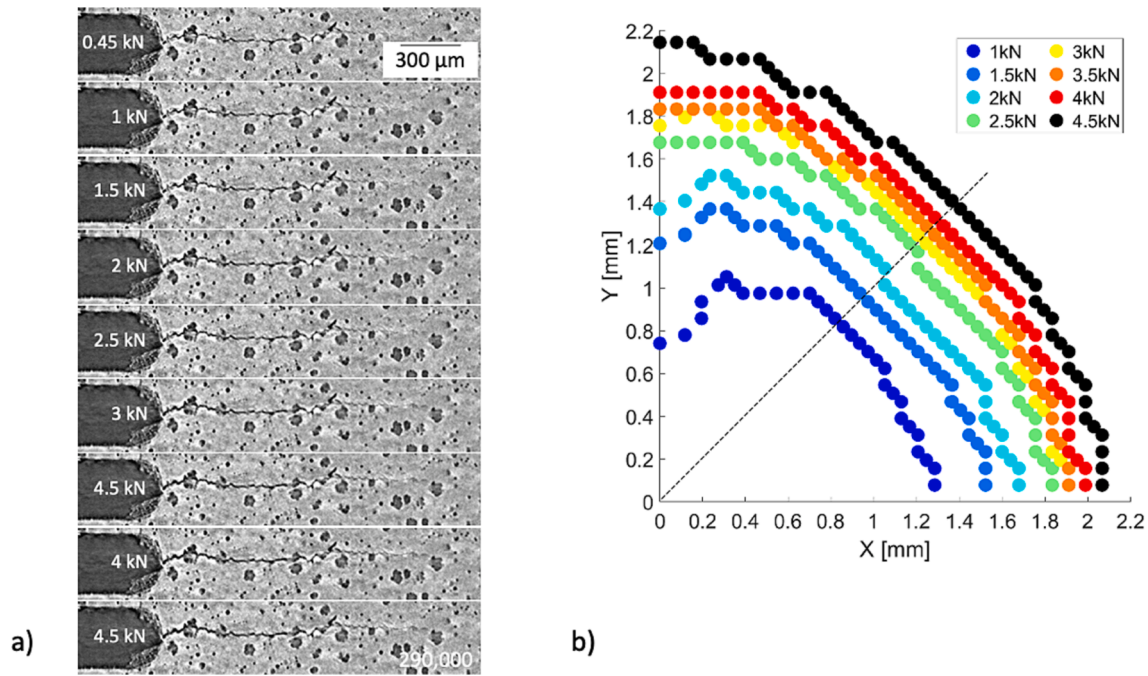


**Fig. 9.** The crack observed in one cycle after 290,000 load cycles at the end of Stage I: a) series of tomograph sections at  $\theta = 45^\circ$  from  $P_{\min}$  (0.45 kN) to  $P_{\max}$  (4.5 kN); b) the position of the open crack tip, identified using phase congruency of the displacement field, as a function of the applied load.

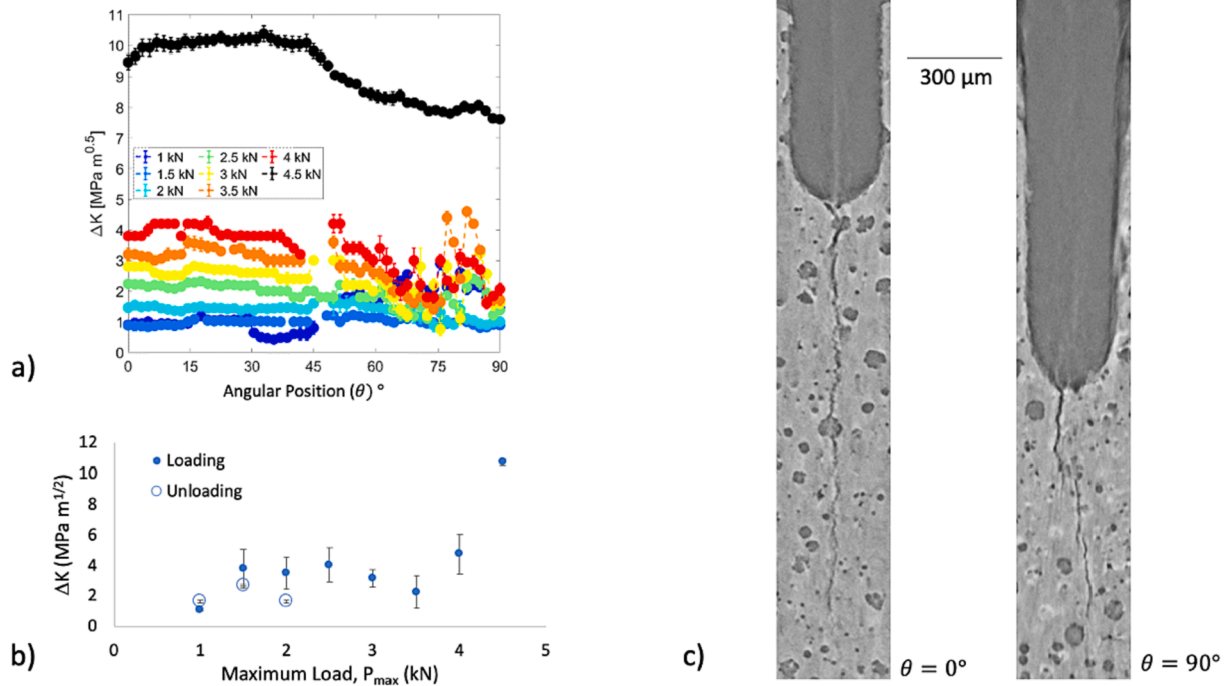


**Fig. 10.** The value of the local mode I stress intensity factor range,  $\Delta K_I$  in one cycle after 290,000 load cycles at the end of Stage I (relative to  $P_{\min}$  0.45 kN): a) as a function of angular position  $\theta$  along the crack front; b) at the angular position  $\theta = 45^\circ$  as a function of applied load with loading and unloading; c) sections of the crack close to the surface at  $\theta = 0^\circ$  and  $\theta = 90^\circ$  at  $P_{\max}$  (4.5 kN) at 290,000 cycles.

the specimen cross-section, load range and crack dimensions (obtained by phase congruency). This is compared with the local data in both Fig. 11a and b, using the average crack growth rate (i.e. the rate of change with cycles of the average crack dimension). The relationship is close to the local data obtained at angular positions approaching  $90^\circ$  (Fig. 11a). The local data obtained at 290,000 cycles for  $\Delta K_I$ , calculated from the change between 4 and 4.5 kN, show a lower  $\Delta K_I$  for similar

crack growth rates than the standard relation (Fig. 11b).

#### 4. Discussion

These observations show that in situ computed tomography with high energy and high brilliance synchrotron X-rays is capable of imaging a mm-scale fatigue crack in a 5 mm thick ferrous specimen, without any



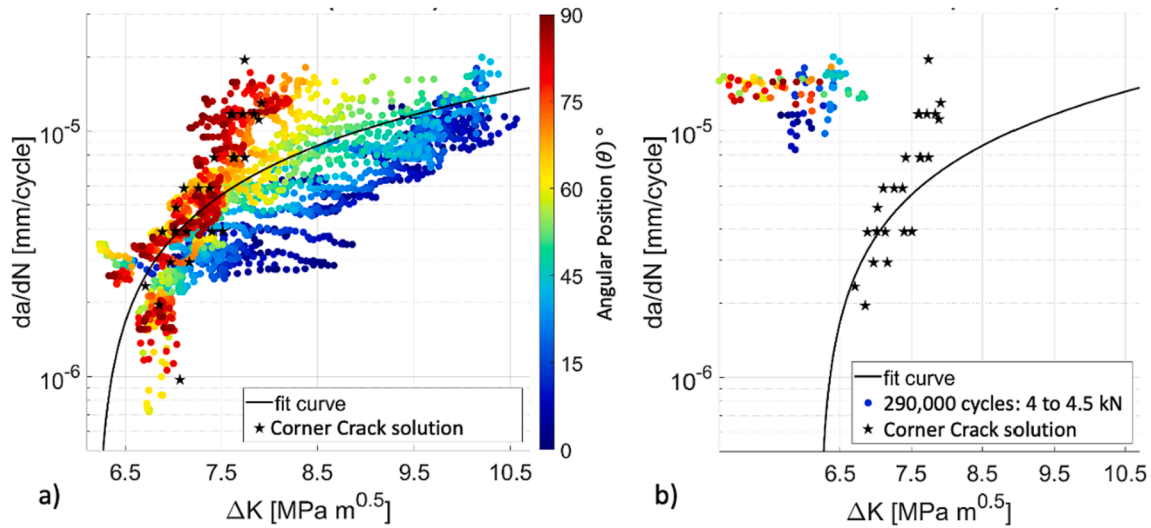


**Fig. 11.** The variation of local crack growth rate,  $da/dN$  with the mode I stress intensity factor range: a) where  $\Delta K_I$  is evaluated between  $P_{\min}$  (0.45 kN) and  $P_{\max}$  (4.5 kN) - the curve has been fitted to the full dataset ('fit curve') for the Paris-Erdogan fatigue equation ( $\frac{da}{dN} = A(\Delta K - \Delta K_{th})^P$ ) for a threshold  $\Delta K_{th}$  of  $6.2 \text{ MPa m}^{1/2}$  determined by manual inspection, with  $A = 4.4 \times 10^{-6}$  and  $P = 0.81$ ; b) the crack growth rate at  $\sim 290,000$  cycles (Fig. 6) as a function of the change in  $K_I$  between 4 and 4.5 kN, with the fitted curve from a) for comparison. The data are colour-coded as a function of angular position  $\theta$ . The stars show the average crack growth rate as a function of the stress intensity factor range predicted for a corner crack under tensile loading ('corner crack solution').

special treatment for the limited angle observations that were a consequence of using a conventional mechanical loading frame. The crack was well resolved at  $3.24 \mu\text{m}$  voxel size when imaged at the maximum load (Fig. 2 and Fig. 3). The phase congruency of the displacement field was quite sensitive to the opening of the crack. This provided an objective measurement of the crack tip position that was consistent with the visible observation of the crack by attenuation contrast (Fig. 5a). This then allowed measurements of the crack dimensions and their change in situ with fatigue cycling and crack propagation. The crack became less visible at lower loads (Fig. 9a), and the position of its open tip varied with load (Fig. 9a) as the crack opening reduced.

The fatigue crack initiated from an asymmetric corner notch and evolved into a semi-circular shape (Fig. 5b), initially with a higher growth rate towards one edge of the notch before the propagation rate along the crack front became essentially independent of the angular position (Fig. 6). This is expected for a fatigue crack loaded in pure mode I, i.e. in a well-aligned test specimen where the applied loads were orthogonal to the notch plane and parallel to the specimen axis. The dimensions of the crack are relatively large compared to the micro-structure, as is the resolution of the crack tip position due to the DVC/phase congruency analysis, so effects such as interactions with grain boundaries and the graphite nodule distribution are not resolvable.

The DVC measurements of the displacement field between maximum and minimum load confirmed that the crack was loaded in pure mode I with negligible shear (Fig. 4). The displacement fields were measured with sufficient resolution and scale to extract stress intensity factors via the finite element method, using these displacements as the local boundary conditions (Fig. 7). The analysis assumed linear elastic properties, although the actual elastic properties of nodular cast iron are non-linear (e.g. a  $\sim 25\%$  reduction in Young modulus with a tensile strain of  $\sim 3\%$  has been reported [41]). A preliminary analysis [2] of the tomographs recorded at 290,000 cycles used a non-linear finite element model with the nodal displacements imported from DVC measurements to extract the variation of the J-integral at several points around the crack front and found a higher J-integral at one surface than in the interior ( $\theta=45^\circ$ ). Non-linear properties could be included in the finite element method here, but their introduction would have a relatively small effect on the magnitude of the stress fields that determine the strain energy of the J-integral, so a linear model has been employed.

This study aimed to evaluate the relationship between the local stress

intensity factor range and crack growth rate. It might be expected that the data would fit a Paris-Erdogan type relationship that was independent of the position along the crack tip, i.e. a measurement of the intrinsic fatigue properties of the material. However, when  $\Delta K_I$  was calculated using the displacement field change between the minimum and maximum loads, the relationship between crack growth rate and  $\Delta K_I$  strongly depended on the angular position around the crack front (Fig. 11a). This indicates that an analysis using only the change in the displacement field between minimum and maximum load is not properly representative of the local crack tip conditions that are responsible for fatigue crack propagation (i.e. the effective stress intensity factor range).

The observations as the load varied over one cycle of the crack at 290,000 cycles show a change in the crack tip visibility (Fig. 9a), the position of the open crack tip (Fig. 9a) and also  $\Delta K_I$  (Fig. 10b). This can be attributed to the effects of compressive crack closure stresses. The plane strain cyclic plastic zone size is small, and of the order of  $15 \mu\text{m}$  (estimated at a stress intensity factor range of  $\sim 10 \text{ MPa m}^{1/2}$ , for a yield stress of  $\sim 300 \text{ MPa}$  [37]). However, the residual stress developed after the applied tensile loading and local plastic deformation at the strain concentration of the notch would act over a larger length scale, and in the unloaded state would compress the crack surfaces. The crack cannot close perfectly due to its roughness, but as the crack opening is small compared to the  $\mu\text{XCT}$  voxel size, the crack tip region became less visible (lower contrast) due to its reduced effect on the local X-ray attenuation [45]. The DVC analysis of the displacements is also sensitive to the opening of the crack [23]. As the applied tensile load increased within the load cycle, the magnitude of the residual compressive stress reduced; this would have the effect of increasing the opening of the imperfectly closed crack to increase its visibility (Fig. 9) and apparent length (Fig. 9b).

The non-linear increase in  $K_I$  with increasing load (Fig. 10b) indicates that the crack was fully open when the applied load was above 4 kN; at lower loads, the crack tip was closed by the compressive residual stress, which decreased in magnitude as the applied tensile stress increased. In the unloaded state, the compressive residual stress would cause the local  $K_I$  to be negative. The displacement fields that were used to calculate  $\Delta K_I$  in Fig. 8 were measured relative to the observation at minimum load, so a reduction in residual compressive stress would cause a gradual increase in  $\Delta K_I$  with increasing load as the local  $K_I$

became less negative. This is consistent with the behaviour in Fig. 10a, and a significant change in  $\Delta K_I$  with load only occurred once the compressive stresses were overcome and the crack tip opened. The crack tip opening determines the local strains that are responsible for fatigue crack growth [2], so the effective change in local  $K_I$  that occurs between high loads when the crack is fully open should control the local crack growth rate. This is supported by the observation that the effective change in  $K_I$  between 4 and 4.5 kN was approximately constant along the crack front, as was the crack growth rate (Fig. 11b). Due to the intervals between the loads at which observations were made, the magnitude of the effective local  $\Delta K_I$  in the fatigue cycle may be systematically underestimated when calculated using the displacement change between 4 and 4.5 kN, since the crack tip may have begun to open at a lower load.

The angular dependence of  $\Delta K_I$  at low loads (i.e. between minimum load and 4 kN) (Fig. 10a) shows its load response varied along the crack front. Noting the change in  $K_I$  that is attributed to tensile relaxation of the compressed, closed crack; this behaviour may be due to spatial variations in either the magnitude of the compressive stress or the compliance of the compressed crack. It has been shown, by X-ray diffraction observations of the elastic strain field of a loaded stress corrosion crack [46], that crack bridging ligaments can significantly restrict the crack opening and reduce the magnitude of the crack tip stress field. Some crack bridging is observed towards the 90° angular position (Fig. 10c), and this may occur due to the lesser degree of crack coalescence with more limited propagation from the longer notch tip. A reduced compliance of the crack due to the mechanical effect of bridging, compared to an open crack, would reduce the magnitude of the displacement field change with load. This might explain the difference between the change in  $\Delta K_I$  with load at low and high  $\theta$  (Fig. 10a) and bridging may also cause some of the observed local variations in  $\Delta K_I$ . However, the asymmetric notch also changes the ligament dimension along the notch front, and the associated variation in tensile stress at the notch tip would affect the magnitude of the notch plastic zone and the consequent residual compressive stress field along the notch tip. More significant residual compressive stress would be expected to occur with the shortest ligament, i.e. at 90°. Noting that the observed bridging is quite local, a variation in the residual compressive stress along the notch is judged to be the more significant factor that causes the observed variation of  $\Delta K_I$  along the notch.

At  $\theta \sim 90^\circ$ , the initial variation of  $\Delta K_I$  with load is much smaller than compared to that at  $\theta \sim 0^\circ$ . A higher magnitude of the compressive residual stresses would reduce the effect of the applied load until the crack became fully open, so in this case, the change in displacement field between the minimum and maximum load is dominated by the displacements associated with the crack tip opening. Hence there is a similarity between the value of  $\Delta K_I$  calculated from the displacement field at  $\theta \sim 90^\circ$  between the minimum and maximum loads (without using any information on the applied loads) and that predicted for the applied loading of a corner crack of similar dimensions (Fig. 11a).

The behaviour in Stage II (crack arrest) and Stage III (crack re-propagation) of the experiment can also be understood as an effect of compressive residual stresses acting on the crack. In Stage II, the effective cyclic opening of the crack tip, represented by  $\Delta K_I$ , was negligible, so no detectable propagation was observed until the more significant loading in Stage III led to a larger crack tip cyclic opening.

In summary, the cyclic change in the opening of the crack tip, which defines the local cyclic strains that govern fatigue crack propagation, can be quantified by measurements of the crack's local displacement field and its parameterisation as a J-integral or stress intensity factor range ( $\Delta K_I$ ). These measurements need to be made when the crack tip is open to obtain the effective stress intensity factor range. Otherwise there can be a systematic error due to displacements caused by the relaxation of compressive stresses that act on a closed crack. A proper assessment of the local conditions of a three-dimensional crack should measure the displacements over the full load cycle to resolve the effects of residual

stress (i.e. crack closure) and other local factors, such as crack bridging.

In heterogeneous microstructures such as nodular cast iron, the local stress intensity factor range can be determined by in situ  $\mu$ XCT with measurement of the displacement field by DVC and parameterisation of this field by J-integral calculation via finite element methods. Strain measurement by synchrotron X-ray diffraction may also be used to quantify the elastic stress intensity factors and investigate the effects of closure and overloads [31]. Many engineering materials have microstructures with more homogeneous patterns of X-ray attenuation and are not suitable for DVC, but different contrast mechanisms are possible. For instance, with Bragg edge neutron tomography [47], suitable features for displacement mapping might be obtained in a polycrystalline structure due to microstructure phase contrast [48,49]. This technique also allows simultaneous mapping of the elastic strains [49,50], which could be used to explore the crack field in more detail. The greater penetration of neutrons, compared to X-rays, could also allow experimental investigations in large components with complex stress states of the local conditions controlling crack propagation. Such studies would be valuable in the verification of predictive models of crack propagation behaviour in industrial applications.

## 5. Conclusions

- In situ three-dimensional observation of the initiation and propagation of a semi-elliptical fatigue crack has been achieved by in situ X-ray tomography, with measurement of the three-dimensional crack shape and displacement field by digital volume correlation.
- The change in the local stress intensity factor with load has been calculated using the displacements as local boundary conditions for a finite element simulation of the crack tip stress field.
- An effect of the residual compressive stresses that cause crack closure can be observed, and it is demonstrated that the local fatigue crack growth rate is determined by the local mode I stress intensity factor range of the fully open crack.

## Declaration of Competing Interest

The authors declare that they have no known competing financial interests or personal relationships that could have appeared to influence the work reported in this paper.

## Data availability

Data will be made available on request.

## Acknowledgement

The award of synchrotron X-ray beamtime at the Diamond Light Source (EE12585) is gratefully acknowledged. This work was facilitated by the University of Oxford John Fell Fund, which supported the Oxford-CNRS Collaboration "Quantitative three-dimensional study of damage in engineering materials".

## References

- [1] McDowell DL, Dunne FPE. Microstructure-sensitive computational modeling of fatigue crack formation. *Int J Fatigue* 2010;32:1521–42. <https://doi.org/10.1016/j.ijfatigue.2010.01.003>.
- [2] Tong J, Alshammrei S, Lin B, Wigger T, Marrow T. Fatigue crack closure: A myth or a misconception? *Fatigue Fract Eng Mater Struct* 2019;42:2747–63. <https://doi.org/10.1111/ffe.13112>.
- [3] Carroll JD, Abuzaid WZ, Lambros J, Sehitoglu H. On the interactions between strain accumulation, microstructure, and fatigue crack behavior. *Int J Fract* 2013; 180:223–41. <https://doi.org/10.1007/s10704-013-9813-8>.
- [4] Christopher CJ, James MN, Patterson EA, Tee KF. Towards a new model of crack tip stress fields. *Int J Fract* 2007;148:361–71. <https://doi.org/10.1007/s10704-008-9209-3>.

- [5] Ritchie RO. Mechanisms of fatigue crack propagation in metals, ceramics and composites: Role of crack tip shielding. *Mater Sci Eng* 1988;103:15–28. [https://doi.org/10.1016/0025-5416\(88\)90547-2](https://doi.org/10.1016/0025-5416(88)90547-2).
- [6] Someday BP, Sofronis P, Nibur KA, San Marchi C, Kirchheim R. Elucidating the variables affecting accelerated fatigue crack growth of steels in hydrogen gas with low oxygen concentrations. *Acta Mater* 2013;61:6153–70. <https://doi.org/10.1016/j.actamat.2013.07.001>.
- [7] Yates JR, Zanganeh M, Tai YH. Quantifying crack tip displacement fields with DIC. *Eng Fract Mech* 2010;77:2063–76. <https://doi.org/10.1016/j.engfracmech.2010.03.025>.
- [8] Tong J, Lin B, Lu Y-W, Madi K, Tai YH, Yates JR, et al. Near-tip strain evolution under cyclic loading: In situ experimental observation and numerical modelling. *Int J Fatigue* 2015;71:45–52. <https://doi.org/10.1016/j.ijfatigue.2014.02.013>.
- [9] Su X, Wan W, Dunne FPE, Marrow TJ. Crack field analysis by optical DIC of short cracks in Zircaloy-4. *Procedia Struct Integrity* 2022;39:663–70. <https://doi.org/10.1016/j.prostr.2022.03.139>.
- [10] Hild F, Roux S. Measuring stress intensity factors with a camera: Integrated digital image correlation (I-DIC); [Mesure de facteurs d'intensité des contraintes avec une caméra : Corrélation d'images numériques intégrée (CINI)]. *Comptes Rendus - Mécanique* 2006;334:8–12. <https://doi.org/10.1016/j.crme.2005.11.002>.
- [11] Lopez-Crespo P, Shterenlikht A, Patterson EA, Yates JR, Withers PJ. The stress intensity of mixed mode cracks determined by digital image correlation. *J Strain Anal Eng Des* 2008;43:769–80. <https://doi.org/10.1243/03093247JSA419>.
- [12] Koko A, Becker TH, Elmukashfi E, Pugno NM, Wilkinson AJ, Marrow TJ. HR-EBSA analysis of in situ stable crack growth at the micron scale. *J Mech Phys Solids* 2023;172:105173. <https://doi.org/10.1016/j.jmps.2022.105173>.
- [13] Friedman LH, Vaudin MD, Stranick SJ, Stan G, Gerbig YB, Osborn W, et al. Assessing strain mapping by electron backscatter diffraction and confocal Raman microscopy using wedge-indented Si. *Ultramicroscopy* 2016;163:75–86. <https://doi.org/10.1016/j.ultramicro.2016.02.001>.
- [14] Steuwer A, Edwards L, Pratihar S, Ganguly S, Peel M, Fitzpatrick ME, et al. In situ analysis of cracks in structural materials using synchrotron X-ray tomography and diffraction. *Nucl Instrum Methods Phys Res, Sect B* 2006;246:217–25. <https://doi.org/10.1016/j.nimb.2005.12.063>.
- [15] Steuwer A, Rahman M, Shterenlikht A, Fitzpatrick ME, Edwards L, Withers PJ. The evolution of crack-tip stresses during a fatigue overload event. *Acta Mater* 2010;58:4039–52. <https://doi.org/10.1016/j.actamat.2010.03.013>.
- [16] Belnoue JP, Jun T-S, Hofmann F, Abbey B, Korsunsky AM. Evaluation of the overload effect on fatigue crack growth with the help of synchrotron XRD strain mapping. *Eng Fract Mech* 2010;77:3216–26. <https://doi.org/10.1016/j.engfracmech.2010.08.018>.
- [17] Marrow TJ, Mostafavi M, Hashimoto T, Thompson GE. A quantitative three-dimensional in situ study of a short fatigue crack in a magnesium alloy. *Int J Fatigue* 2014;66:183–93. <https://doi.org/10.1016/j.ijfatigue.2014.04.003>.
- [18] Herbig M, King A, Reischig P, Proudhon H, Lauridsen EM, Marrow J, et al. 3-D growth of a short fatigue crack within a polycrystalline microstructure studied using combined diffraction and phase-contrast X-ray tomography. *Acta Mater* 2011;59:590–601. <https://doi.org/10.1016/j.actamat.2010.09.063>.
- [19] King A, Ludwig W, Herbig M, Buffière J-Y, Khan AA, Stevens N, et al. Three-dimensional in situ observations of short fatigue crack growth in magnesium. *Acta Mater* 2011;59:6761–71. <https://doi.org/10.1016/j.actamat.2011.07.034>.
- [20] Rannou J, Limodin N, Réthoré J, Gravouil A, Ludwig W, Baietto-Dubourg M-C, et al. Three dimensional experimental and numerical multiscale analysis of a fatigue crack. *Comput Methods Appl Mech Eng* 2010;199:1307–25. <https://doi.org/10.1016/j.cma.2009.09.013>.
- [21] Lachambre J, Réthoré J, Weck A, Buffière J-Y. Extraction of stress intensity factors for 3D small fatigue cracks using digital volume correlation and X-ray tomography. *Int J Fatigue* 2015;71:3–10. <https://doi.org/10.1016/j.ijfatigue.2014.03.022>.
- [22] Williams ML. On the Stress Distribution at the Base of a Stationary Crack. *J Appl Mech* 1957;24:109–14. <https://doi.org/10.1115/1.4011454>.
- [23] Jin X, Wade-Zhu J, Chen Y, Mummery PM, Fan X, Marrow TJ. Assessment of the fracture toughness of neutron-irradiated nuclear graphite by 3D analysis of the crack displacement field. *Carbon* 2021;171:882–93. <https://doi.org/10.1016/j.carbon.2020.09.072>.
- [24] Cinar AF, Barhli SM, Hollis D, Flansbjerg M, Tomlinson RA, Marrow TJ, et al. An autonomous surface discontinuity detection and quantification method by digital image correlation and phase congruency. *Opt Lasers Eng* 2017;96:94–106. <https://doi.org/10.1016/j.optlaseng.2017.04.010>.
- [25] Barhli SM, Saucedo-Mora L, Jordan MSL, Cinar AF, Reinhard C, Mostafavi M, et al. Synchrotron X-ray characterization of crack strain fields in polygranular graphite. *Carbon* 2017;124:357–71. <https://doi.org/10.1016/j.carbon.2017.08.075>.
- [26] Becker TH, Molteni MR, Marrow TJ. Procedure for accurate calculation of the J-Integral from digital volume correlation displacement data. *Strain* 2020. <https://doi.org/10.1111/str.12337>.
- [27] Barhli SM, Hollis D, Wieneke B, Mostafavi M, Marrow TJ. Advanced 2D and 3D Digital Image Correlation of the Full-Field Displacements of Cracks and Defects. *ASTM Evaluation of Existing and New Sensor Technologies for Fatigue, Fracture and Mechanical Testing* 2014. <https://doi.org/10.1520/STP158420140052>.
- [28] Breitharth E, Strohm T, Besel M, Reh S. Determination of Stress Intensity Factors and J integral based on Digital Image Correlation. *Frattura Ed Integrità Strutturale* 2019;13:12–25. <https://doi.org/10.3221/IGF-ESIS.49.02>.
- [29] Barhli SM, Mostafavi M, Cinar AF, Hollis D, Marrow TJ. J-Integral Calculation by Finite Element Processing of Measured Full-Field Surface Displacements. *Exp Mech* 2017;57:997–1009. <https://doi.org/10.1007/s11340-017-0275-1>.
- [30] Becker TH, Mostafavi M, Tait RB, Marrow TJ. An approach to calculate the J-integral by digital image correlation displacement field measurement. *Fatigue Fract Eng Mater Struct* 2012;97:1–84. <https://doi.org/10.1111/j.1460-2695.2012.01685.x>.
- [31] Koko A, Earp P, Wigger T, Tong J, Marrow TJ. J-Integral Analysis: An EDXD and DIC Comparative Study for a Fatigue Crack. *Int J Fatigue* 2020;105:474. <https://doi.org/10.1016/j.ijfatigue.2020.105474>.
- [32] Parks DM. The virtual crack extension method for nonlinear material behavior. *Comput Methods Appl Mech Eng* 1977;12:353–64. [https://doi.org/10.1016/0045-7825\(77\)90023-8](https://doi.org/10.1016/0045-7825(77)90023-8).
- [33] Jin X, Marrow TJ, Wang J, Chen Y, Chen H, Scotson D, et al. Crack propagation in fine grained graphites under mode I and mixed-mode loading, as observed in situ by microtomography. *Carbon* 2022. <https://doi.org/10.1016/j.carbon.2022.03.051>.
- [34] Yan L, Cinar A, Ma S, Abel R, Hansen U, Marrow TJ. A method for fracture toughness measurement in trabecular bone using computed tomography, image correlation and finite element methods. *J Mech Behav Biomed Mater* 2020;109:103838. <https://doi.org/10.1016/j.jmbbm.2020.103838>.
- [35] Shih CF, Asaro RJ. Elastic-Plastic Analysis of Cracks on Bimaterial Interfaces: Part I—Small Scale Yielding. *J Appl Mech* 1988;55:299–316. <https://doi.org/10.1115/1.3173676>.
- [36] Limodin N, Réthoré J, Buffière J-Y, Gravouil A, Hild F, Roux S. Crack closure and stress intensity factor measurements in nodular graphite cast iron using three-dimensional correlation of laboratory X-ray microtomography images. *Acta Mater* 2009;57. <https://doi.org/10.1016/j.actamat.2009.05.005>.
- [37] Limodin N, Réthoré J, Buffière J-Y, Hild F, Roux S, Ludwig W, et al. Influence of closure on the 3D propagation of fatigue cracks in a nodular cast iron investigated by X-ray tomography and 3D volume correlation. *Acta Mater* 2010;58:2957–67. <https://doi.org/10.1016/j.actamat.2010.01.024>.
- [38] Marrow TJ, Buffière JY, Withers PJ, Johnson G, Engelberg DL. High resolution X-ray tomography of short fatigue crack nucleation in austempered ductile cast iron. *Int J Fatigue* 2004;26:717–25. <https://doi.org/10.1016/j.ijfatigue.2003.11.001>.
- [39] Drakopoulos M, Connolly T, Reinhard C, Atwood R, Magdysyuk O, Vo N, et al. I12: The Joint Engineering, Environment and Processing (JEEP) beamline at Diamond Light Source. *J Synchrotron Radiat* 2015;22:828–38. <https://doi.org/10.1107/S1600577515003513>.
- [40] Mostafavi M, Collins DM, Cai B, Bradley R, Atwood RC, Reinhard C, et al. Yield behavior beneath hardness indentations in ductile metals, measured by three-dimensional computed X-ray tomography and digital volume correlation. *Acta Mater* 2015;82:468–82. <https://doi.org/10.1016/j.actamat.2014.08.046>.
- [41] Tomicevic Z, Kodvanj J, Hild F. Characterization of the nonlinear behavior of nodular graphite cast iron via inverse identification—Analysis of uniaxial tests. *Eur J Mech A Solids* 2016;59:140–54. <https://doi.org/10.1016/j.euromechsol.2016.02.010>.
- [42] Allen RJ, Booth GS, Jutla T. A review of fatigue crack growth characterisation by linear elastic fracture mechanics (LEFM). Part II—Advisory documents and applications within National Standards. *Fatigue Fract Eng Mater Struct* 1988;11:71–108. <https://doi.org/10.1111/j.1460-2695.1988.tb01162.x>.
- [43] Raju I, Newman I. Stress-intensity factors for corner cracks in rectangular bars. In: Cruse TA, editor. *Fracture Mechanics: Nineteenth Symposium*. STP969-EB ed., ASTM International; 1988. <https://doi.org/10.1520/STP969-EB>.
- [44] ASTM International. ASTM E740/E740M-03 Standard Practice for Fracture Testing with Surface-Crack Tension Specimens. 2016. doi:10.1520/E0740-E0740M-03R16.
- [45] Bull DJ, Sinclair I, Spearing SM. Partial volume correction for approximating crack opening displacements in CFRP material obtained from micro-focus X-ray CT scans. *Compos Sci Technol* 2013;81:9–16. <https://doi.org/10.1016/j.compscitech.2013.03.017>.
- [46] Marrow TJ, Steuwer A, Mohammed F, Engelberg D, Sarwar M. Measurement of crack bridging stresses in environment-assisted cracking of duplex stainless by synchrotron diffraction. *Fatigue Fract Eng Mater Struct* 2006;29:464–71. <https://doi.org/10.1111/j.1460-2695.2006.01019.x>.
- [47] Reid A, Marshall M, Kabra S, Minniti T, Kockelmann W, Connolly T, et al. Application of neutron imaging to detect and quantify fatigue cracking. *Int J Mech Sci* 2019;159:182–94. <https://doi.org/10.1016/j.ijmecsci.2019.05.037>.
- [48] Woracek R, Penmadu D, Kardjilov N, Hilger A, Boin M, Banhart J, et al. Neutron Bragg Edge Tomography for Phase Mapping. *Phys Procedia* 2015;69:227–36. <https://doi.org/10.1016/j.phpro.2015.07.032>.
- [49] Woracek R, Penmadu D, Kardjilov N, Hilger A, Strobl M, Wimpory RC, et al. Neutron Bragg-edge-imaging for strain mapping under in situ tensile loading. *J Appl Phys* 2011;109:93506. <https://doi.org/10.1063/1.3582138>.
- [50] Busi M, Polatidis E, Malamud F, Kockelmann W, Morgano M, Kaestner A, et al. Bragg edge tomography characterization of additively manufactured 316L steel. *Phys Rev Materials* 2022;6:53602. <https://doi.org/10.1103/PhysRevMaterials.6.053602>.